Evaluating the macroscopic yield behaviour of trabecular bone using a nonlinear homogenisation approach

JOURNAL OF THE MECHANICAL BEHAVIOR OF BIOMEDICAL MATERIALS 61 (2016) 384–396

Available online at www.sciencedirect.com

ScienceDirect

www.elsevier.com/locate/jmbbm

Research Paper

Evaluating the macroscopic yield behaviour of trabecular bone using a nonlinear homogenisation approach

Francesc Levrero-Florencio[a,*], *Lee Margetts*[b], *Erika Sales*[a], *Shuqiao Xie*[a], *Krishnagoud Manda*[a], *Pankaj Pankaj*[a]

[a]*Institute for Bioengineering, School of Engineering, The University of Edinburgh, Faraday Building, King's Buildings, EH9 3JG Edinburgh, United Kingdom*

[b]*School of Mechanical, Aerospace and Civil Engineering, University of Manchester, Oxford Road, M13 9PL Manchester, United Kingdom*

ARTICLE INFO

Article history:
Received 3 September 2015
Received in revised form
28 March 2016
Accepted 6 April 2016
Available online 13 April 2016

Keywords:
Finite Elements
Anisotropic Material
Yield Surface
Multiscale Modelling
Trabecular Bone

ABSTRACT

Computational homogenisation approaches using high resolution images and finite element (FE) modelling have been extensively employed to evaluate the anisotropic elastic properties of trabecular bone. The aim of this study was to extend its application to characterise the macroscopic yield behaviour of trabecular bone. Twenty trabecular bone samples were scanned using a micro-computed tomography device, converted to voxelised FE meshes and subjected to 160 load cases each (to define a homogenised multiaxial yield surface which represents several possible strain combinations). Simulations were carried out using a parallel code developed in-house. The nonlinear algorithms included both geometrical and material nonlinearities. The study found that for tension-tension and compression-compression regimes in normal strain space, the yield strains have an isotropic behaviour. However, in the tension-compression quadrants, pure shear and combined normal-shear planes, the macroscopic strain norms at yield have a relatively large variation. Also, our treatment of clockwise and counter-clockwise shears as separate loading cases showed that the differences in these two directions cannot be ignored. A quadric yield surface, used to evaluate the goodness of fit, showed that an isotropic criterion adequately represents yield in strain space though errors with orthotropic and anisotropic criteria are slightly smaller. Consequently, although the isotropic yield surface presents itself as the most suitable assumption, it may not work well for all load cases. This work provides a comprehensive assessment of material symmetries of trabecular bone at the macroscale and describes in detail its macroscopic yield and its underlying microscopic mechanics.

Abbreviations: (FE), Finite element; (CT), Computed tomography; (MIL), Mean interceptlength; (RVE), Representative volume element; (MPI), Message passing interface

*Corresponding author.
E-mail address: f.levrero-florencio@ed.ac.uk (F. Levrero-Florencio).

http://dx.doi.org/10.1016/j.jmbbm.2016.04.008

1. Introduction

Exponential growth of older population implies that problems associated with deteriorated mechanical capabilities of bone need urgent attention. Computational modelling to examine the mechanical response of musculoskeletal systems requires the mechanical behaviour of bone to be defined satisfactorily (Pankaj, 2013). A continuum description of bone that can be related to its microstructure and includes its anisotropy and its yield behaviour will go a long way in predicting failure of bone and bone-implant systems.

The macroscopic elastic behaviour of bone has been mostly modelled using isotropic linear elasticity. Often, bone macroscopic properties are assumed to be homogeneous with separate elastic properties being assigned to cortical and trabecular bone (Completo et al., 2009; Conlisk et al., 2015). Sometimes, subject specific macroscopic elastic properties are assigned using computed tomography (CT) scans, which permit inhomogeneity in the material properties on the basis of CT attenuations (Helgason et al., 2008; Schileo et al., 2008; Tassani et al., 2011). That said, since CT attenuations can only provide scalar values, assumption of isotropy needs to be made. However, it is well recognised that the macroscopic behaviour of bone is not isotropic. For trabecular bone, which resembles open cell foams, the anisotropy is largely a consequence of its anisotropic microarchitecture (Odgaard et al., 1997; Turner et al., 1990). An ultrasonic approach proposed by van Buskirk et al. (1981) was shown to provide a good approximation of nine orthotropic elastic constants if a heterogeneity correction were included. In general, experimental mechanical techniques are unable to provide the complete stiffness tensor at the resolution required for modelling (Odgaard et al., 1989).

Image based computational approaches have been successfully applied for the evaluation of the macroscopic stiffness tensors (Donaldson et al., 2011; van Rietbergen et al., 1995). In these, micro-CT (or micro-magnetic resonance imaging) scans of bone are converted into high resolution 3D finite element (FE) meshes, with a detailed geometry of its microstructure. The solid phase (or bone tissue) is assigned isotropic elastic properties and the volume element (VE) is then computationally subjected to six strain/stress states (three normal and three shear). The response enables evaluation of the full macroscopic elastic stiffness tensor using the standard mechanics methodology (van Rietbergen et al., 1996). Previous studies have extensively employed these homogenisation approaches, and relationships between stiffness and microarchitectural indices (volume fraction and fabric tensor) have also been established (Cowin, 1986; Turner and Cowin, 1987; Turner et al., 1990; Zysset and Curnier, 1995).

While modelling bone as an elastic material may be adequate for a few applications, a significant proportion of applications requires evaluation of post-elastic response, e.g. to evaluate implant loosening resulting in its failure. Many studies still continue to employ elastic analyses to predict arbitrarily post-elastic behaviour (Falcinelli et al., 2014).

Both stress- and strain-based criteria have been used to describe the macroscopic yield surface of bone (Keaveny et al., 1994; Keller, 1994; Kopperdahl and Keaveny, 1998). In recent years a consensus appears to be emerging that strain-based criteria are easier to apply as trabecular bone behaviour in this space is "more isotropic" and density independent than in stress space (Bayraktar et al., 2004; Chang et al., 1999; Pankaj and Donaldson, 2013). There is also now some evidence to suggest that failure of bone is strain-controlled rather than stress-controlled (Nalla et al., 2003). However, there is little consensus on the yield criterion that may be suitable for this cellular material.

Homogenisation techniques, using micro-CT images and FE analyses, that have been successful in the elastic domain, require huge computational resources in the plastic regime for a number of reasons: nonlinear homogenisation requires a large number of load cases (unlike the linear elastic regime which only requires six); nonlinear simulations require considerably more computational effort; and to capture nonlinear phenomena FE meshes need to be finer. As a consequence, nonlinear homogenisation to obtain the macroscopic yield criterion of bone requires high performance computing and has been attempted only by a few previous studies (Bayraktar et al., 2004; Sanyal et al., 2015; Wolfram et al., 2012). All these studies used a simple bilinear criterion to represent the solid phase of bone. Wolfram et al. (2012) used a limited number of load cases which can lead to loss of information on physiologically possible complex load cases, while both Sanyal et al. (2015) and Wolfram et al. (2012) made a priori assumptions with regard to macroscopic yield surface symmetries; the former assumed it to be transverse isotropic and the latter orthotropic.

Nanoindentation experiments on bone suggest that the solid phase of bone has a pressure-dependent yield surface (i.e. its yielding depends on hydrostatic stress), which arises because of bone's cohesive-frictional behaviour (Tai et al., 2006). Due to this reason, bone tissue (or the solid phase) can be modelled using classical criteria, such as Mohr-Coulomb or Drucker-Prager (Carnelli et al., 2010; Tai et al., 2006).

On the macroscale, high density bone is prone to tissue yielding, while low density bone is likely to fail via a mixture of large deformation failure mechanisms and tissue yielding (Bevill et al., 2006; Morgan et al., 2004; Stolken and Kinney, 2003). At the microscale, total strains can be large and a small strain approximation may be invalid. It is important to note that local yielding or buckling may not imply simultaneous yielding of the homogenised structure; the latter results from a significantly compromised stress carrying capacity.

The aim of this study is to characterise the macroscopic yield surface of trabecular bone by using a numerical homogenisation approach, derived from multiscale theory (de Souza Neto et al., 2015; Kruch and Chaboche, 2011; McDowell, 2010): using high resolution FE meshes obtained from micro-CT images; applying a range of load cases which adequately describes the multiaxial behaviour of bone at the macroscale (including complex normal and shear load combinations); incorporating both geometrical and material nonlinearities; and with a validated pressure sensitive yield criterion for the solid phase. We consider a range of trabecular bone densities and also examine the efficacy of quadric surfaces as representatives for its macroscopic yield surface.

2. Material and methods

The tensorial notation used in this study largely follows the notation used by Schwiedrzik et al. (2013). A first-order tensor (or vector) is denoted by a lowercase bold letter (e.g. **m**), a second-order tensor is denoted by an uppercase bold letter (e.g. **A**) and a fourth-order tensor is denoted by a double-barred uppercase letter (e.g. $\mathbb{A}$). The tensor operations which will appear throughout the text are: single contraction of two second-order tensors, e.g. **AB** (or $A_{ik}B_{kj}$ in indicial notation); double contraction of two second-order tensors, e.g. $\mathbf{A} : \mathbf{B}$ ($A_{ij}B_{ij}$); double contraction of a fourth-order tensor and a second-order tensor, e.g. $\mathbb{A} : \mathbf{B}$ ($\mathbb{A}_{ijkl}B_{kl}$); double contraction of a second-order tensor and a fourth-order tensor, e.g. $\mathbf{B} : \mathbb{A}$ ($B_{ij}\mathbb{A}_{ijkl}$); tensor product of two first-order tensors, e.g. $\mathbf{m} \otimes \mathbf{m}$ ($m_i m_j$); tensor product of two second-order tensors, e.g. $\mathbf{A} \otimes \mathbf{B}$ $(A_{ij}B_{kl})$; and the symmetric tensor product of two second-order tensors, e.g. $\mathbf{A} \bar{\otimes} \mathbf{B}$ $(\frac{1}{2}[A_{ik}B_{jl} + A_{il}B_{jk}])$.

2.1. *Imaging and finite element meshing*

Ten trabecular bone specimens were extracted from bovine trochanters and femoral heads (young cattle, <2.5 years old). Coarse micro-CT images of the central femoral head and trochanter regions were taken for three specimens prior to coring. All subsequent samples were then cored with respect to the visually ascertained trabecular directions. The extracted cylindrical specimens had a diameter of 10.7 mm and a length of 29.9 mm. Diamond-tipped cores (Starlite Industries, Rosemont PA, USA) were used in the extraction of the specimens and the top and bottom edges of the cores were cut with a slow speed saw (Isomet 1000, Buehler, Düsseldorf, Germany) by using a diamond wafering blade designed for bone. All these procedures were performed under constant irrigation to avoid excessive abrasion and overheating.

The specimens were submerged into phosphate buffered saline and scanned using micro-CT (Skyscan 1172, Bruker, Zaventern, Belgium) with a resolution of 17.22 μm. The scanning parameters were 94 kV, 136 mA and 200 ms integration time; 4 scans in 720 equiangular radial positions which were averaged. The grey scale images were binarised with an automatic thresholding script (Gomez et al., 2013).

Twenty virtual cubes of 5 mm length were extracted from the scanned and segmented cylinders. The Mean Intercept Length (MIL) fabric tensor (Harrigan and Mann, 1984) was evaluated using BoneJ (Doube et al., 2010) and then used to align the coordinate axes of the images with the eigenvectors of the fabric. This approach has been employed in a recent study (Wolfram et al., 2012). After the 5 mm cubes were cropped, the alignment was rechecked to ensure that there was no misalignment larger than 8° (Sanyal et al., 2015; Wolfram et al., 2012). MIL is known to approximate the elastic orthotropic directions of trabecular bone (Odgaard, 1997). By undertaking such alignment there was an expectation that these axes may also represent the orthotropic directions of the yield criterion if the criterion was orthotropic. The bone tissue volume (solid phase) over total volume ratios (BV/TV) had a range from 13.7% to 30.3%. The degree of anisotropy of these cubes, which is the ratio between the largest and smallest eigenvalues of the fabric tensor, ranged from 1.52 to 3.86. A 5 mm length Volume Element (VE) which has been previously considered appropriate to capture the features of trabecular bone (Harrigan et al., 1988; Sanyal et al., 2015; van Rietbergen et al., 1995) was employed for all simulations.

2.2. *Constitutive model and computational procedure*

The twenty specimens were meshed using a voxelised mesh, where every voxel corresponds to a trilinear hexahedron, with an in-house developed script that meshes in parallel using the Message Passing Interface (MPI) (Forum, 1994). The meshing procedure was performed using 30 cores on a cluster at The University of Edinburgh, which is called Eddie (Edinburgh Compute and Data Facilities, ECDF). The largest

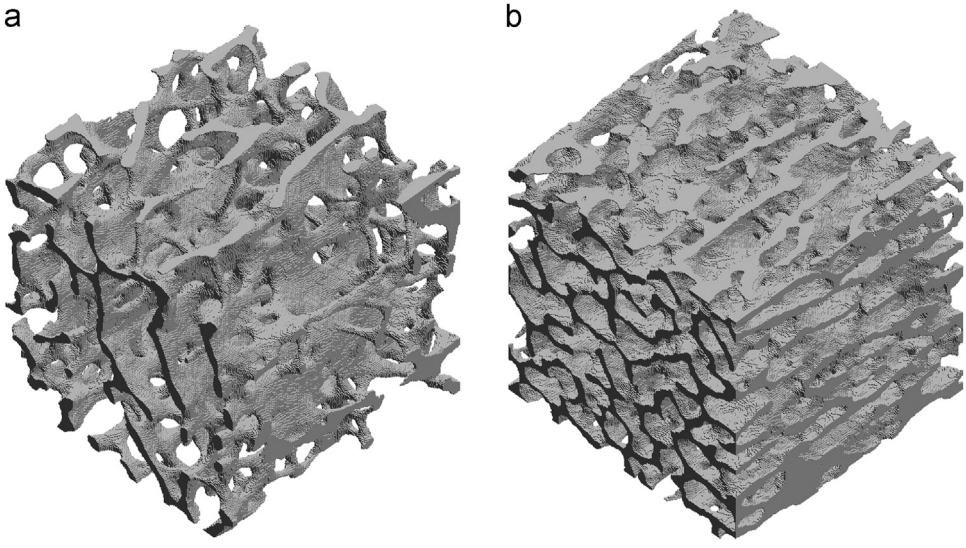

Fig. 1 – FE meshes of the most porous sample (13.7% BV/TV) (left) and of the densest sample (30.3% BV/TV) (right). Both samples are cubes of 5 mm edge length.

mesh had around 9 million nodes. FE models for two of the twenty specimens are shown in Fig. 1.

The solid phase was modelled as an isotropic elastoplastic material. It is important to mention that trabecular bone at the tissue level is actually transverse isotropic or orthotropic (Hellmich et al., 2004; Malandrino et al., 2012; Wolfram et al., 2010). However, as pointed out by Cowin (1997), there is little to no error in assuming tissue isotropy. This is because the trabecula are composed of laminated material about their axes, which implies transverse isotropy or orthotropy; since the axis of the trabecula is the same as the loading axis, a beam made of orthotropic material can be reduced to a beam made of isotropic material.

The elastic regime was modelled using Hencky hyperelasticity, which restricts this material model to isotropic, with a Poisson's ratio of 0.3 and a Young's Modulus of 12700 MPa (Wolfram et al., 2012). A quadric yield surface (Schwiedrzik et al., 2013) given by

$$G(\tau) = \sqrt{\tau:\mathbb{G}:\tau} + \mathbf{G}:\tau - 1 = 0 \tag{1}$$

was employed, where τ is the Kirchhoff stress and $\mathbb{G}$ and $\mathbf{G}$ are, respectively, a fourth-order tensor and a second-order tensor defined by

$$\mathbb{G} = -\zeta_0 G_0^2(\mathbf{I}\otimes\mathbf{I}) + (\zeta_0+1)G_0^2\left(\mathbf{I}\bar{\otimes}\mathbf{I}\right) \tag{2}$$

and

$$\mathbf{G} = \frac{1}{2}\left(\frac{1}{\sigma_0^+} - \frac{1}{\sigma_0^-}\right)\mathbf{I} \tag{3}$$

where

$$G_0 = \frac{\sigma_0^+ + \sigma_0^-}{2\sigma_0^+\sigma_0^-} \tag{4}$$

and $\mathbf{I}$ is the second-order unit tensor, σ_0^+ and σ_0^- are the tensile and compressive yield stresses, respectively, and ζ_0 is an interaction parameter.

Eq. (1) approximates a Drucker-Prager criterion when $\zeta_0 = 0.49$. Recent studies using indentation tests on bone tissue have suggested that the solid phase of bone can be represented using a Drucker-Prager type criterion (Carnelli et al., 2010; Tai et al., 2006). Uniaxial yield strains of 0.41% in tension and 0.83% in compression (Bayraktar and Keaveny, 2004) were converted to yield stresses by simply multiplying them by the Young's modulus of the solid phase (Schwiedrzik et al., 2015). Although there have been some experimental studies that have evaluated hardening of the extracellular matrix (Luczynski et al., 2015; Schwiedrzik et al., 2014), there is no agreement on the solid phase hardening behaviour of trabecular bone. Some studies have assumed linear hardening (Bayraktar and Keaveny, 2004; Bevill et al., 2006). In this study perfect plasticity was assumed (Carnelli et al., 2010), though small hardening (0.02% of the Young's modulus) was included to aid prevention of loss of ellipticity. In order to ensure global convergence of the Newton-Closest Point Projection Method (Newton-CPPM) scheme, a line search procedure was implemented as in the primal-CPPM algorithm proposed by Perez-Foguet and Armero (2002).

Each cubic specimen was subjected to 160 strain-controlled load cases as described in Table 1. The boundary conditions used to constrain the VE were kinematic uniform boundary conditions applied as described by Wang et al. (2009). It is recognised that these boundary conditions provide an upper bound for trabecular bone stiffness and also for yield (Panyasantisuk et al., 2015; Wang et al., 2009). The simulations were run on a Cray XC30 supercomputer hosted by ARCHER, the UK National Supercomputing Service. The analyses were carried out with an in-house parallel implicit finite strain solver, developed within the context of ParaFEM (Margetts, 2002; Smith et al., 2014), which uses an Updated Lagrangian formulation. This code uses MPI to perform the parallelisation (Smith and Margetts, 2003, 2006). The high scalability of the code has already been demonstrated in previous work (Levrero Florencio et al., 2015; Margetts et al., 2015). Each of the 160 simulations per sample took approximately 12 min using 1920 cores; therefore the total number of core hours employed in this study is approximately 1.2 million.

A Newton-Raphson scheme was used as the solution tracking technique and a preconditioned conjugate gradient solver was used to solve the resulting linear algebraic systems. They are fast and if there are any convergence problems, they arise from the same origin (e.g. due to loss of positive definiteness of the stiffness matrix). However, convergence problems were only encountered in few of the porous samples (in 20 out of 3200 simulations) and can be related to a limit point or large-deformation related failure mechanisms (Bevill et al., 2006; de Souza Neto et al., 2008).

Table 1 – Description of the load cases undertaken. Clockwise and counter-clockwise shear are differentiated by the sign of the off-diagonal terms of the homogeneous strain: clockwise corresponds to positive sign and counter-clockwise corresponds to negative sign. If T and C represent tension and compression respectively in normal strain space and clockwise and counter-clockwise shear in shear strain space, then the quadrants comprise of C-C, T-T, C-T and T-C; and octants comprise of C-C-C, C-C-T, C-T-C, C-T-T, T-C-C, T-C-T, T-T-C and T-T-T.

Type of analysis		Number of analyses
Uniaxial normal	3 tensile and 3 compressive	6
Uniaxial shear	3 clockwise and 3 counter-clockwise	6
Biaxial normal	3 planes, 1 analysis per quadrant	12
Triaxial normal	8 octants, 1 analysis per octant	8
Biaxial shear	3 planes, 1 analysis per quadrant	12
Triaxial shear	8 octants, 1 analysis per octant	8
Biaxial normal-shear	9 planes, 1 analysis per quadrant	36
Biaxial normal-shear with different ratios	9 planes, 2 analysis per quadrant	72
	Total	160

These points were marked differently in the figures and included in the fitting procedure as yield points.

The initial load increment size corresponded to 0.1% macroscopic strain norm and could decrease to a minimum of 0.001% if global convergence was not achieved in larger load increments.

3. Theory and calculation

3.1. Definition of the macroscopic yield points

The yield points were described in the plane where the abscissa is the Frobenius norm of the applied macroscopic strain, which corresponds to the Green-Lagrange strain, and the ordinate is the Frobenius norm of the homogenised Second Piola-Kirchhoff stress (Fig. 2), described by

$$\mathbf{S}_{\text{hom}} = \frac{1}{V_0}\sum_{i=1}^{nel}\sum_{j=1}^{nip} w_i \det\mathbf{J}_{ij}\mathbf{S}_{ij} \tag{5}$$

where there is no summation implied on repeated indices, V_0 is the initial volume of the VE, nel is the number of elements in the FE simulation, nip is the number of Gauss integration points in a trilinear hexahedra, **J** is the Jacobian, **S** is the Second-Piola Kirchhoff stress and w are the weights corresponding to the specific Gauss integration point.

The 0.2% criterion was used to define the yield points (Wolfram et al., 2012), as shown in Fig. 2, and the elastic slope was obtained from the first two load increments, which were always fully elastic.

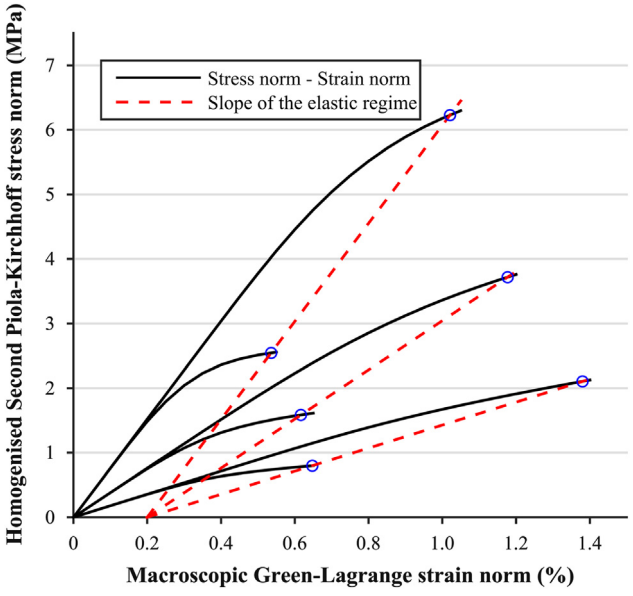

Fig. 2 – Determination of the yield points by using the 0.2% criterion for the tensile and compressive uniaxial load cases of one sample. As it can be seen, the tensile and compressive uniaxial cases have the same elastic slope (dashed red line), as expected.

3.2. Formulation for macroscopic yield surface

Although a key aim of this study was to assess how different bone samples yield when subjected to the wide array of 160 load cases, we also examined the macroscopic yield surface fit using a quadric surface. The choice was based on its simplicity, because it has been previously related to the fabric tensor of bone (Cowin, 1986; Wolfram et al., 2012), and because it is a smooth surface.

The quadric yield surface is described in strain space as

$$Y(\mathbf{E}) = \sqrt{\mathbf{E} : \mathbb{F} : \mathbf{E}} + \mathbf{F} : \mathbf{E} - 1 = 0 \tag{6}$$

where **E** is the Green-Lagrange strain tensor, $\mathbb{F}$ and **F** are used to define the shape, directionality and eccentricity of the yield surface. $\mathbb{F}$ is a fourth-order tensor, which has major and minor symmetries ($\mathbb{F}_{ijkl} = \mathbb{F}_{klij}$ and $\mathbb{F}_{ijkl} = \mathbb{F}_{jikl} = \mathbb{F}_{ijlk} = \mathbb{F}_{jilk}$), allowing it to be defined on a symmetric matrix space (Sym^6), by 21 coefficients (Mehrabadi and Cowin, 1990). As stated in Schwiedrzik et al. (2013), convexity of Eq. (6) is ensured with positive semi-definiteness of $\mathbb{F}$. **F** is a symmetric second-order tensor, thus being described by 6 coefficients.

3.3. Different symmetries of the yield surface

Three different cases were investigated: isotropy, orthotropy and full anisotropy. Details about isotropic and orthotropic formulations can be found in (Schwiedrzik et al., 2013); only anisotropy is discussed in the following.

In the case of full anisotropy, or triclinic symmetry, the material can have different shear yield strains clockwise and counter-clockwise. For an anisotropic quadric, normal strains can interact with shear strains and shear strains can interact amongst themselves (Theocaris, 1992; Tsai and Wu, 1971). This means that in the triclinic case, $\mathbb{F}$ and **F** have 21 and 6 independent coefficients respectively.

By performing uniaxial strain load cases, several coefficients of $\mathbb{F}$ and all the coefficients of **F** can be determined. For **F**, the coefficients are

$$\mathbf{F}_{ij} = \begin{cases} \frac{1}{2}\left(\frac{1}{\varepsilon_{ij}^{+}} - \frac{1}{\varepsilon_{ij}^{-}}\right) \text{if } i = j \\ \frac{1}{4}\left(\frac{1}{\varepsilon_{ij}^{+}} - \frac{1}{\varepsilon_{ij}^{-}}\right) \text{if } i \neq j \end{cases} \quad i,j = 1,2,3 \tag{7}$$

In the case of $\mathbb{F}$, the six diagonal coefficients of the projection of $\mathbb{F}$ onto Sym^6 are

$$\mathbb{F}_{ijij} = \begin{cases} \left(\frac{\varepsilon_{ij}^{+}+\varepsilon_{ij}^{-}}{2\varepsilon_{ij}^{+}\varepsilon_{ij}^{-}}\right)^2 \text{if } i = j \\ \frac{1}{2}\left(\frac{\varepsilon_{ij}^{+}+\varepsilon_{ij}^{-}}{2\varepsilon_{ij}^{+}\varepsilon_{ij}^{-}}\right)^2 \text{if } i \neq j \end{cases} \quad i,j = 1,2,3 \tag{8}$$

The 15 remaining parameters to be determined correspond to three normal strain interaction parameters, three shear strain interaction parameters and nine normal-shear strain interaction parameters. These parameters have expressions in the coefficients of $\mathbb{F}$ which are related to the previously stated diagonal coefficients, as shown in Table 2.

These, together with the six uniaxial normal strains and six uniaxial shear strains, add up to a total of 27 parameters. Calculating the determinant of 1×1 and 2×2 principal minors of the projection of $\mathbb{F}$ onto Sym^6 allows establishment

Table 2 – Interaction coefficients for the anisotropic quadric.

	Coefficient
Normal interaction	$\mathbb{F}_{1122}=\zeta_{12}\left(\frac{\varepsilon_{11}^{+}+\varepsilon_{11}^{-}}{2\varepsilon_{11}^{+}\varepsilon_{11}^{-}}\right)\left(\frac{\varepsilon_{22}^{+}+\varepsilon_{22}^{-}}{2\varepsilon_{22}^{+}\varepsilon_{22}^{-}}\right)$
	$\mathbb{F}_{1133}=\zeta_{13}\left(\frac{\varepsilon_{11}^{+}+\varepsilon_{11}^{-}}{2\varepsilon_{11}^{+}\varepsilon_{11}^{-}}\right)\left(\frac{\varepsilon_{33}^{+}+\varepsilon_{33}^{-}}{2\varepsilon_{33}^{+}\varepsilon_{33}^{-}}\right)$
	$\mathbb{F}_{2233}=\zeta_{23}\left(\frac{\varepsilon_{22}^{+}+\varepsilon_{22}^{-}}{2\varepsilon_{22}^{+}\varepsilon_{22}^{-}}\right)\left(\frac{\varepsilon_{33}^{+}+\varepsilon_{33}^{-}}{2\varepsilon_{33}^{+}\varepsilon_{33}^{-}}\right)$
Shear interaction	$\mathbb{F}_{1213}=\zeta_{45}\left(\frac{\varepsilon_{12}^{+}+\varepsilon_{12}^{-}}{2\varepsilon_{12}^{+}\varepsilon_{12}^{-}}\right)\left(\frac{\varepsilon_{13}^{+}+\varepsilon_{13}^{-}}{2\varepsilon_{13}^{+}\varepsilon_{13}^{-}}\right)$
	$\mathbb{F}_{1223}=\zeta_{46}\left(\frac{\varepsilon_{12}^{+}+\varepsilon_{12}^{-}}{2\varepsilon_{12}^{+}\varepsilon_{12}^{-}}\right)\left(\frac{\varepsilon_{23}^{+}+\varepsilon_{23}^{-}}{2\varepsilon_{23}^{+}\varepsilon_{23}^{-}}\right)$
	$\mathbb{F}_{1323}=\zeta_{56}\left(\frac{\varepsilon_{13}^{+}+\varepsilon_{13}^{-}}{2\varepsilon_{13}^{+}\varepsilon_{13}^{-}}\right)\left(\frac{\varepsilon_{23}^{+}+\varepsilon_{23}^{-}}{2\varepsilon_{23}^{+}\varepsilon_{23}^{-}}\right)$
Normal-shear interaction	$\mathbb{F}_{1112}=\zeta_{14}\left(\frac{\varepsilon_{11}^{+}+\varepsilon_{11}^{-}}{2\varepsilon_{11}^{+}\varepsilon_{11}^{-}}\right)\left(\frac{\varepsilon_{12}^{+}+\varepsilon_{12}^{-}}{2\varepsilon_{12}^{+}\varepsilon_{12}^{-}}\right)$
	$\mathbb{F}_{1113}=\zeta_{15}\left(\frac{\varepsilon_{11}^{+}+\varepsilon_{11}^{-}}{2\varepsilon_{11}^{+}\varepsilon_{11}^{-}}\right)\left(\frac{\varepsilon_{13}^{+}+\varepsilon_{13}^{-}}{2\varepsilon_{13}^{+}\varepsilon_{13}^{-}}\right)$
	$\mathbb{F}_{1123}=\zeta_{16}\left(\frac{\varepsilon_{11}^{+}+\varepsilon_{11}^{-}}{2\varepsilon_{11}^{+}\varepsilon_{11}^{-}}\right)\left(\frac{\varepsilon_{23}^{+}+\varepsilon_{23}^{-}}{2\varepsilon_{23}^{+}\varepsilon_{23}^{-}}\right)$
	$\mathbb{F}_{2212}=\zeta_{24}\left(\frac{\varepsilon_{22}^{+}+\varepsilon_{22}^{-}}{2\varepsilon_{22}^{+}\varepsilon_{22}^{-}}\right)\left(\frac{\varepsilon_{12}^{+}+\varepsilon_{12}^{-}}{2\varepsilon_{12}^{+}\varepsilon_{12}^{-}}\right)$
	$\mathbb{F}_{2213}=\zeta_{25}\left(\frac{\varepsilon_{22}^{+}+\varepsilon_{22}^{-}}{2\varepsilon_{22}^{+}\varepsilon_{22}^{-}}\right)\left(\frac{\varepsilon_{13}^{+}+\varepsilon_{13}^{-}}{2\varepsilon_{13}^{+}\varepsilon_{13}^{-}}\right)$
	$\mathbb{F}_{2223}=\zeta_{26}\left(\frac{\varepsilon_{22}^{+}+\varepsilon_{22}^{-}}{2\varepsilon_{22}^{+}\varepsilon_{22}^{-}}\right)\left(\frac{\varepsilon_{23}^{+}+\varepsilon_{23}^{-}}{2\varepsilon_{23}^{+}\varepsilon_{23}^{-}}\right)$
	$\mathbb{F}_{3312}=\zeta_{34}\left(\frac{\varepsilon_{33}^{+}+\varepsilon_{33}^{-}}{2\varepsilon_{33}^{+}\varepsilon_{33}^{-}}\right)\left(\frac{\varepsilon_{12}^{+}+\varepsilon_{12}^{-}}{2\varepsilon_{12}^{+}\varepsilon_{12}^{-}}\right)$
	$\mathbb{F}_{3313}=\zeta_{35}\left(\frac{\varepsilon_{33}^{+}+\varepsilon_{33}^{-}}{2\varepsilon_{33}^{+}\varepsilon_{33}^{-}}\right)\left(\frac{\varepsilon_{13}^{+}+\varepsilon_{13}^{-}}{2\varepsilon_{13}^{+}\varepsilon_{13}^{-}}\right)$
	$\mathbb{F}_{3323}=\zeta_{36}\left(\frac{\varepsilon_{33}^{+}+\varepsilon_{33}^{-}}{2\varepsilon_{33}^{+}\varepsilon_{33}^{-}}\right)\left(\frac{\varepsilon_{23}^{+}+\varepsilon_{23}^{-}}{2\varepsilon_{23}^{+}\varepsilon_{23}^{-}}\right)$

of basic restrictions on some of the coefficients to ensure that $\mathbb{F}$ is positive semi-definite, which are

$$\varepsilon_{ij}^{\pm}\geq 0;|\zeta_{kl}|\leq 1;i,j=1,2,3;k,l=1,2,\ldots,6 \tag{9}$$

The remaining restrictions on the coefficients are not expressed analytically but checked after the minimisation procedure to ensure positive semi-definiteness of $\mathbb{F}$. For every symmetry case and for every sample, the eigenvalues of the projection of $\mathbb{F}$ onto Sym^6 were checked to ensure they were non-negative.

3.4. *Evaluating goodness of fit*

The macroscopic yield envelope was fitted by using a minimisation procedure in MATLAB (Mathworks, Natick MA, USA). To evaluate the goodness of fit, the error was evaluated as

$$\text{Fitting error}=\frac{1}{N}\sum_{i=1}^{N}\frac{\|\mathbf{E}_{\text{fitted}}-\mathbf{E}_{\text{FE}}\|}{\|\mathbf{E}_{\text{FE}}\|} \tag{10}$$

where $\|\cdot\|$ is the Frobenius norm of the corresponding macroscopic strain and N is the cardinality of a specific set of load cases. This error was evaluated for four different sets: for all the load cases; for the load cases which entirely lie on the normal strain space; for the load cases which entirely lie on the shear strain space; and for the strain cases that have one component in the normal strain space and one component in the shear strain space (which from now onwards will be referred to as combined normal and shear strain space).

4. Results

4.1. *Macroscopic yield strains*

Macroscopic yield points in strain space for all twenty considered samples in the normal-normal and shear-shear planes are shown in Fig. 3. These represent 36 of the 160 load cases analysed for each sample, and no projections have been made, i.e. the yield strains only contain out-of-plane components equal to zero. Results show that the macroscopic yield surface of bone has a higher yield strain in compression than in tension in the normal strain space. This is expected due to the characteristics of its solid phase.

It can be seen that the tensile quadrant displays quasi-uniform macroscopic yield strains across samples (upper right quadrant of Fig. 3a, b, c). The compressive yield strains have some variability across samples, as can be seen from the spread of yield points in the lower left quadrant of Fig. 3a, b, c. The largest variation in the normal-normal planes is in the tensile-compressive quadrants (upper left and lower right quadrants, Fig. 3a, b, c).

Macroscopic yield strains in the shear-shear planes show a large variation of yield strains for different specimens (Fig. 3d, e, f). It can also be observed that the shear yield strains of bone are different in clockwise and counter-clockwise directions, with these absolute differences ranging from 0.0034% to 0.4463%. A statistical comparison between these yield strains was performed for all pure shear cases with a paired t-test. This test suggests that paired clockwise and counter-clockwise shear yield strains are statistically different ($p<0.01$).

Macroscopic uniaxial (tensile, compressive and shear) yield strains were related to BV/TV and fabric through multi-linear regressions performed in log space. No relationship between yield strains and BV/TV and fabric was found. Only compressive uniaxial yield strains were mildly related to BV/TV and fabric ($R^2=0.44$, $p\rightarrow 0$).

In order to examine macroscopic yield strains in tension-tension, compression-compression and tension-compression regimes, we evaluated the mean of the macroscopic Green Lagrange strain norm for each of the above three regimes, as shown in Fig. 4. As expected, the mean of the norms is the lowest for tension-tension, highest for compression-compression and in between for tension-compression. Fig. 4 also shows the standard deviation in the evaluated norms. It can be observed that the deviation is relatively small for the tension-tension regime, higher for compression-compression regime and the highest for tension-compression regime.

4.2. *Solid phase strains*

We examined strains at the microscale (solid phase strains). Under uniaxial macroscopic tension, more localised strains were found to occur at the solid phase level, and there were mostly no compressive solid phase strains anywhere in the specimens. However, under uniaxial macroscopic compression, the compressive solid phase strains were more diffused and found to occur throughout the geometry. Further, under macroscopic compression, large tensile solid phase strains

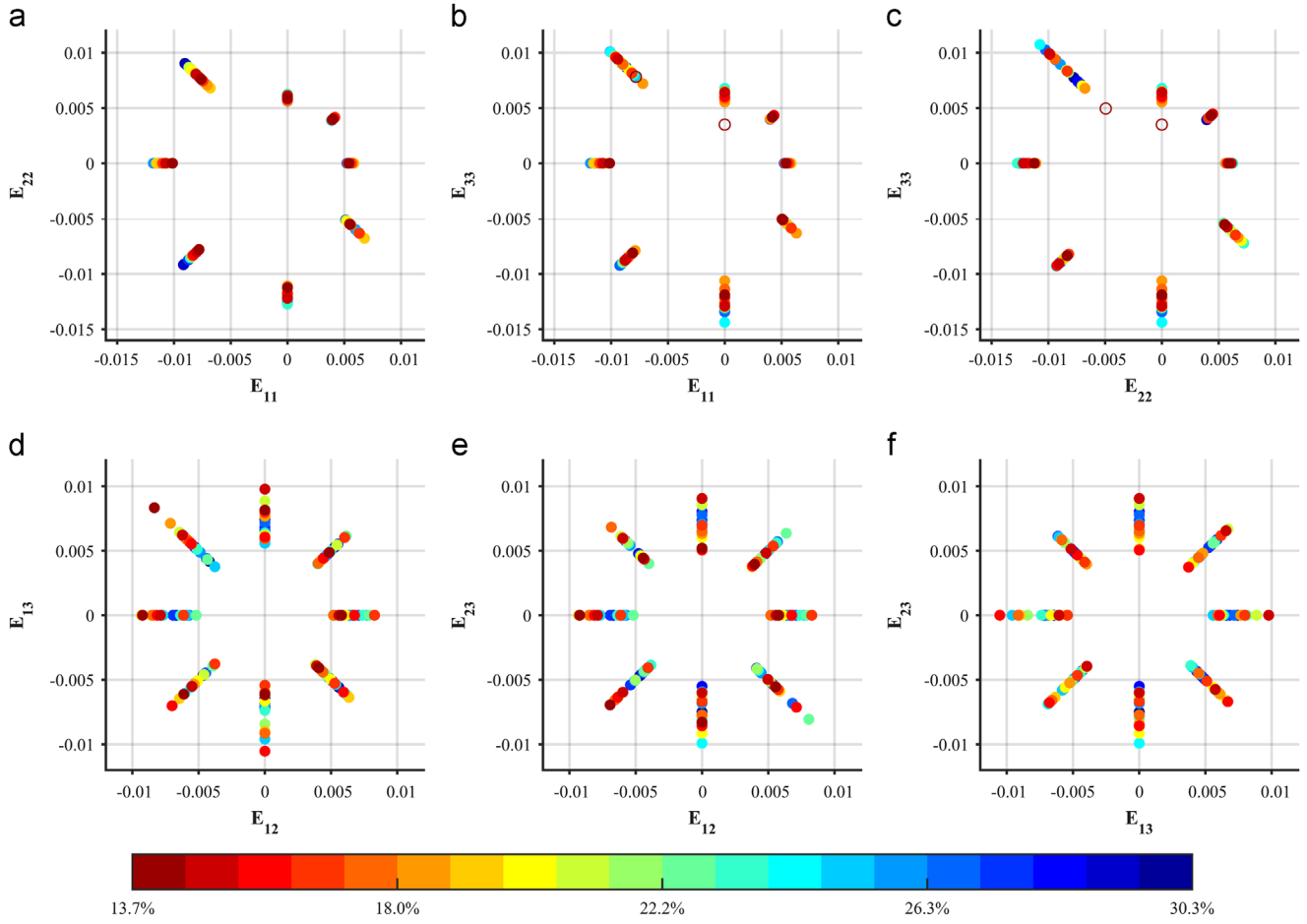

Fig. 3 – Macroscopic yield points of the 20 specimens in normal strain planes (a, b, c) and in shear strain planes (d, e, f). In the shear strain planes, clockwise shear is represented as positive and counter-clockwise shear is represented as negative. Density of the samples is indicated by the colour-bar. Yield points obtained for a few cases from the loss of positive definiteness of the stiffness matrix are marked with an empty circle.

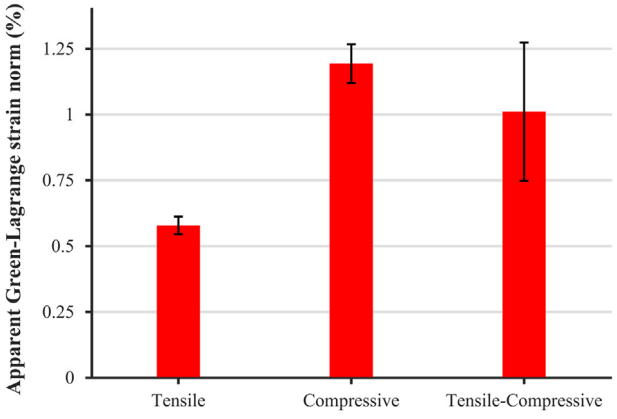

Fig. 4 – Bar plot of the mean of the macroscopic Green Lagrange strain norms for tensile cases (i.e. cases in the normal strain space where all strain components are positive), compressive cases (i.e. cases in the normal strain space where all strain components are negative) and tensile-compressive cases (i.e. cases in the normal strain space where one component is positive and one component is negative). The error bars correspond to the standard deviation of these values.

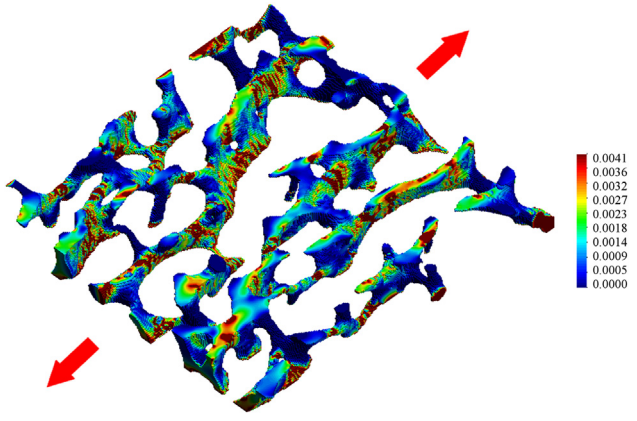

Fig. 5 – Distribution of the Green-Lagrange solid phase strain component E_{11} for a 0.5x5 × 5 mm slice of bone under macroscopic uniaxial tension. Direction 1 is in the direction denoted by the arrows.

were found to arise, due to bending and buckling of trabeculae. Fig. 5 and Fig. 6 show this for a slice from one typical porous sample.

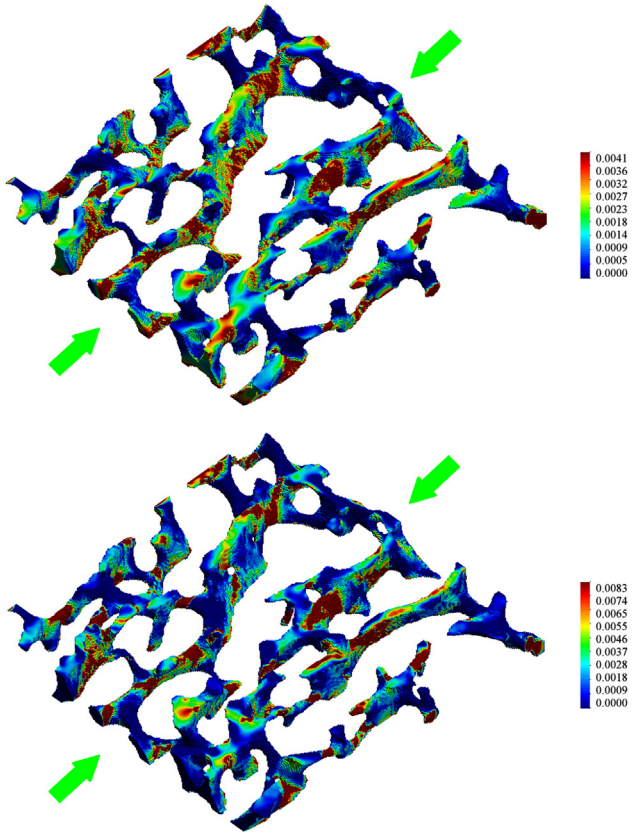

Fig. 6 – Distribution of the Green-Lagrange solid phase strain under macroscopic uniaxial compression for a 0.5x5 × 5 mm slice of bone. Tensile component E_{22} (top) and compressive component E_{11} (bottom). Direction 1 is in the direction denoted by the arrows and direction 2 is the orthogonal in-plane direction.

4.3. *Macroscopic yield surface and fitting errors*

A macroscopic yield surface was fitted for each of the 20 samples by using isotropic, orthotropic and fully anisotropic quadric yield surfaces, using all of the 160 load cases. The parameters for the anisotropic surface have been added as a statistical evaluation in Table 3. Plots for the two samples with the highest and lowest densities are shown in Fig. 7. The lower density sample shows a higher level of anisotropy in comparison to the higher density sample. Further, if consecutive macroscopic yield points of the porous sample are joined up, then the homogenised yield envelope does not always remain entirely convex in some of the planes (e.g. Fig. 7i, k).

Mean fitting errors (Eq. (10) considering all samples and all strain cases are shown in Fig. 8. It can be seen that the isotropic assumption leads to the highest (~11%) error, followed by the orthotropic (~10%) and the anisotropic (~8%) assumptions. The standard deviation of the fitting errors is also shown in the figure and it can be seen that the error variation across densities with the isotropic assumption is similar to the orthotropic case; the anisotropic assumption produces the smaller variations across samples.

Table 3 – Statistical evaluation of the parameters of the anisotropic surface.

Coefficient	Value (mean ± standard deviation)
$\mathbb{F}_{1111}$	18391.8±5092.2
$\mathbb{F}_{1122}$	7801.1±1056.9
$\mathbb{F}_{1133}$	8492.1±1021.2
$\mathbb{F}_{1112}$	155.5±866.8
$\mathbb{F}_{1113}$	306.6±1883.35
$\mathbb{F}_{1123}$	150.0±684.1
$\mathbb{F}_{2222}$	17510.1±2826.5
$\mathbb{F}_{2233}$	8644.4±1713.2
$\mathbb{F}_{2212}$	−83.4±800.1
$\mathbb{F}_{2213}$	84.0±744.1
$\mathbb{F}_{2223}$	495.5±1619.2
$\mathbb{F}_{3333}$	20689.0±4299.2
$\mathbb{F}_{3312}$	12.2±628.9
$\mathbb{F}_{3313}$	260.1±1616.6
$\mathbb{F}_{3323}$	538.9±1787.2
$\mathbb{F}_{1212}$	4557.3±688.8
$\mathbb{F}_{1213}$	228.2±374.2
$\mathbb{F}_{1223}$	287.8±482.6
$\mathbb{F}_{1313}$	5016.1±724.8
$\mathbb{F}_{1323}$	−3.5±427.7
$\mathbb{F}_{2323}$	5200. 4±844.0
$\mathbf{F}_{11}$	52.6±14.3
$\mathbf{F}_{22}$	52.0±8.2
$\mathbf{F}_{33}$	60.9±12.5
$\mathbf{F}_{12}$	0.4±2.5
$\mathbf{F}_{13}$	0.8±5.1
$\mathbf{F}_{23}$	1.8±4.6

In general, the fitting errors were not found to correlate with bone density (Fig. 9). In normal strain space (Fig. 9a), the assumption of an isotropic quadric led to consistently higher errors, while the orthotropic and anisotropic assumptions resulted in smaller fitting errors. In the shear strain space (Fig. 9b), in the combined normal and shear strain space (Fig. 9c), and in the general strain space (Fig. 9d), the assumption of anisotropic quadric had the smallest errors. A mild trend of errors decreasing with increasing density was observed for the isotropic and orthotropic assumptions in shear strain space. In the general strain space, the errors and the error differences between assumptions tend to reduce with increasing density.

5. Discussion

Our study shows that the macroscopic yield surface of bone in normal strain space is fairly uniform across a wide range of samples; this confirms findings of previous research (Bayraktar et al., 2004; Lambers et al., 2014; Pankaj and Donaldson, 2013).

Our results also demonstrate that the full three-dimensional macroscopic yield behaviour of trabecular bone can be reasonably well described using the isotropic quadric yield surface, though orthotropic and anisotropic surfaces lead to smaller errors. This is in agreement with previous studies in which the strain space yield surface was reported to be isotropic (Bayraktar et al., 2004) and more recently transversely isotropic (Sanyal et al., 2015) and orthotropic (Wolfram et al., 2012). However, unlike the above studies, our

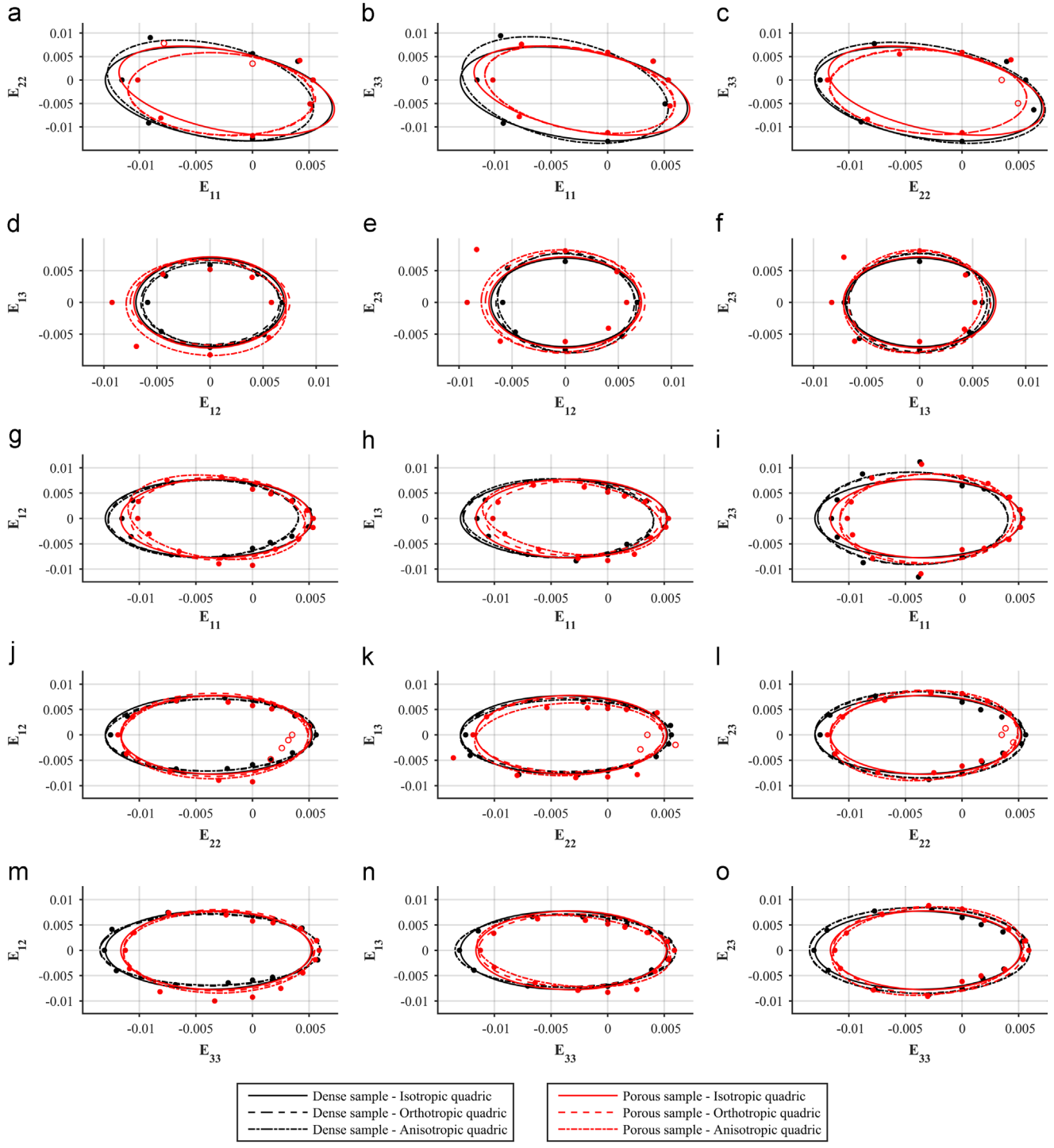

Fig. 7 – Macroscopic yield points for the densest and most porous samples and their corresponding isotropic, orthotropic and anisotropic fitted quadric surfaces in the normal strain planes (a, b, c), shear strain planes (d, e, f), and combined normal and shear strain planes (g–o). Yield points obtained for a few cases from the loss of positive definiteness of the stiffness matrix are marked with an empty circle.

treatment of clockwise and counter-clockwise shears as separate loading cases showed that the differences in the two directions are significant. This is probably because trabeculae are not symmetrically aligned with respect to the axes of the material, which in this case were assessed through the eigenvectors of the MIL fabric tensor. It is important to note that the assumption of identical macroscopic yield points in clockwise and counter-clockwise directions restricts the system to orthotropy at best (Theocaris, 1992; Tsai and Wu, 1971). We also observed predominance of tensile solid phase strains in pure macroscopic shear, which is consistent with Sanyal et al. (2012).

Multilinear regressions suggest that uniaxial yield strains are not correlated with BV/TV and fabric (Matsuura et al.,

2008; Morgan and Keaveny, 2001; Panyasantisuk et al., 2015). Only a mild dependence was found for the uniaxial compressive yield strains (R^2=0.44, $p \to 0$), with a positive slope for density and a negative slope for fabric, which suggests that long trabeculae, i.e. associated with a high fabric eigenvalue, have lower macroscopic yield strain, as suggested by Matsuura et al. (2008). Since no clear relationship between a fabric tensor and the yield strains was found, use of an isotropic yield surface formulation in strain space is more practical for real applications.

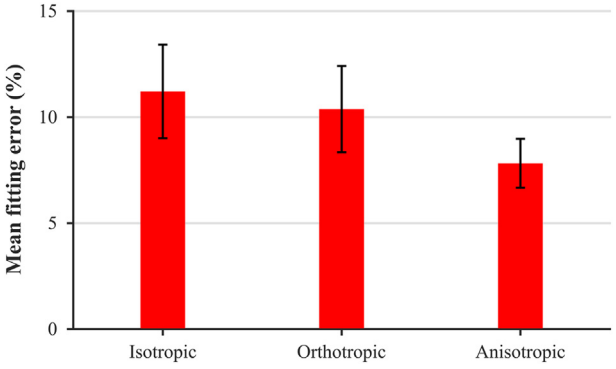

Fig. 8 – Bar plot of the mean of the fitting errors across all samples for the isotropic quadric, orthotropic quadric and anisotropic quadric. All the strain cases are taken into account. The error bars correspond to the standard deviation of these values.

In uniaxial macroscopic tension, solid phase strains are almost exclusively tensile and independent of density (Bayraktar and Keaveny, 2004; Lambers et al., 2014). The highly oriented structure of trabecular bone results in the yield strains at the solid phase and at the macroscale being very similar in tension. When trabecular bone is loaded in macroscopic compression, yield mechanisms are different: in this case, yielding at the solid phase was found to occur both due to tension (arising from bending and buckling of trabeculae) and compression. As expected, we found considerable tensile strains in trabeculae for low density samples as has been previously reported (Bevill et al., 2006; Morgan et al., 2004; Stolken and Kinney, 2003). This density dependence results in macroscopic yield variation being displayed via a small spread of yield points in the compression-compression quadrants (lower left quadrants of Fig. 3a–c), as shown by the mild relationship between compressive uniaxial yield strains and density and fabric. This also implies that solid phase uniaxial yield strain asymmetry is not fully maintained at the macroscale and generally reduces with increased porosity and increased fabric eigenvalues. Our results are consistent with the experimental results of Lambers et al. (2014) in the sense that the number of microscopic yielded sites in macroscopic compression and in macroscopic tension are similar in number, but in macroscopic tension, the microscopic yield zones have more localised strains, which could be related to microcrack propagation.

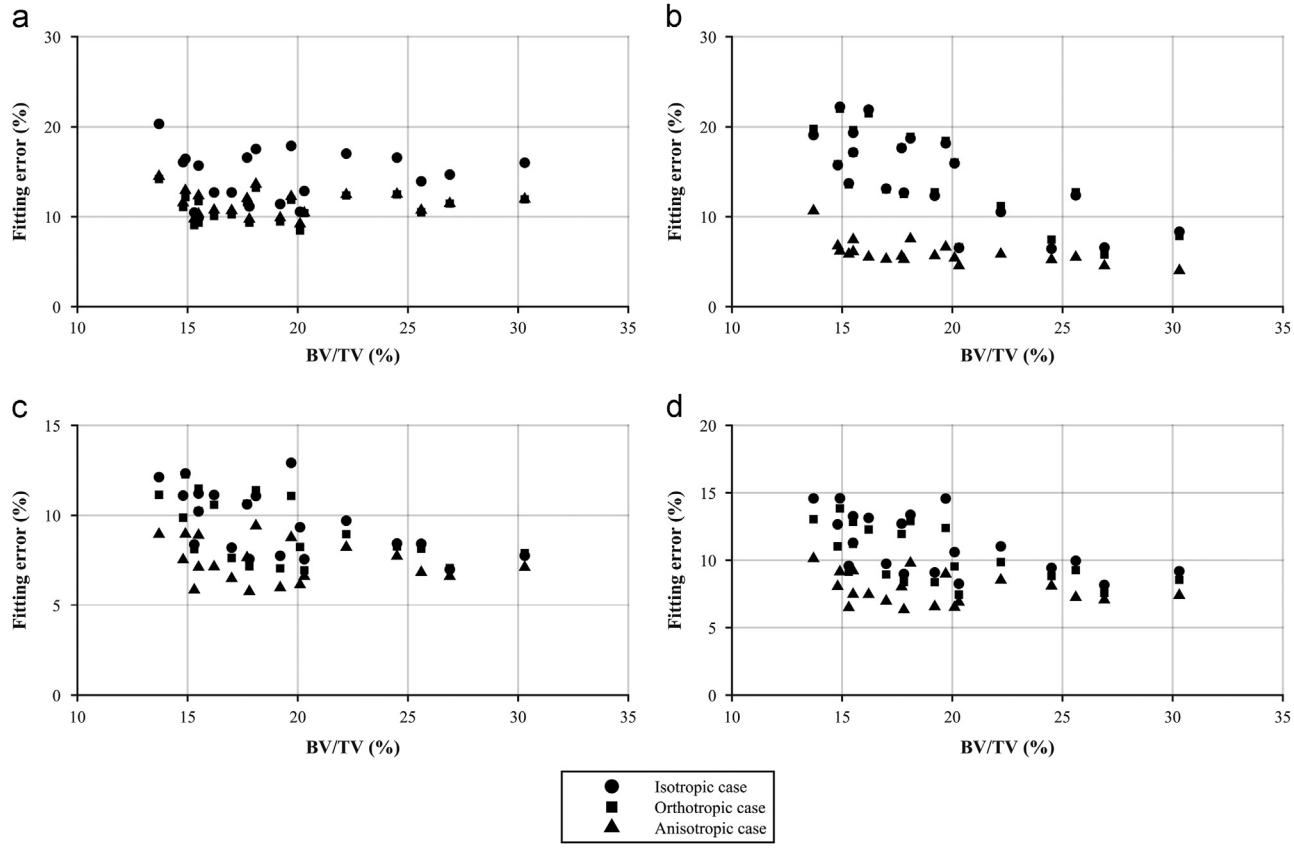

Fig. 9 – Fitting errors as described in eq. 20 for the normal strain space (a), shear strain space (b), combined normal and shear strain space (c) and in general strain space (d).

The few previous studies that have evaluated the macroscale yield surface of bone from its microstructure have all used a bilinear criterion, with yield strain asymmetry, to define the solid phase of bone with a reduced stiffness beyond defined tissue yield values (Bayraktar et al., 2004; Sanyal et al., 2015; Wolfram et al., 2012). In our study, the solid phase of bone was modelled using a Drucker-Prager type criterion which has been validated via experimental studies (Carnelli et al., 2010; Tai et al., 2006). Our study considered yield points arising from 160 different load cases. Some recent studies have been limited to 17 load cases (Panyasantisuk et al., 2015; Wolfram et al., 2012). In order to compare our results we considered 17 strain cases similar to those in the cited studies. We found the errors to be 11.4% for the isotropic case and 10.3% for the orthotropic case for the 17 cases. The errors, taking into account all 160 cases, are 11.2% for the isotropic case, 10.4% for the orthotropic case and 7.8% for the anisotropic case. In other words, the 17 load cases lead to errors of a similar magnitude to those obtained using all 160 load cases. To further examine the effect of the considered load cases on the fitting error, we considered a single sample with different load cases. We evaluated the fitting errors considering all normal load cases proposed by Wolfram et al. (2012) (14 cases) and all our shear cases (26 cases). The errors were 18.0%, 16.3% and 7.6% for isotropic, orthotropic and anisotropic assumptions respectively. With the 17 load cases mentioned previously, the errors reduce to 9.8% and 6.5% for isotropic and orthotropic assumptions respectively for this sample. With all the 160 load cases, the errors are 13.3%, 12.9% and 9.2% for isotropic, orthotropic and anisotropic assumptions respectively. This illustrates that shear cases contribute importantly to anisotropy, and that the fitting errors clearly depend on the considered load cases, which illustrates the importance of examining a large range of complex load cases. With respect to the combined normal and shear strain spaces, the shear component of the macroscopic yield strain is often found to increase when there is a compressive normal component, indicating typical cellular solid behaviour (Fenech and Keaveny, 1999; Gibson and Ashby, 1997).

Our study has a number of limitations. We chose to use a quadric due to its simplicity, because it has been used in previous studies, because it requires fewer parameters than higher order criteria, and because it is a smooth surface, not requiring multiple plastic multipliers. Although our primary aim was to examine the effect of material symmetry assumptions on the macroscopic yield surface, the fitting errors clearly depend on the shape of the chosen surface and on the considered load cases. While we examined full anisotropy with a quadric surface, a previous study employed a higher order polynomial surface, a quartic, but restricted it to transverse isotropy (Sanyal et al., 2015); a restriction that is not fully supported by our results.

Although the solid phase constitutive law has been validated (Carnelli et al., 2010; Tai et al., 2006), there is no experimental validation for the macroscopic yield surfaces. In fact, such a validation is impossible as samples tested once cannot be retested and it is not possible to obtain numerous (or even two) identical samples. There have, however, been some attempts to on trabecular bone wherein the loading cases have been limited to triaxial compression (Keaveny et al., 1999; Rincon-Kohli and Zysset, 2009). Thus, the range of complex strain cases we have tested can only be performed numerically.

We considered homogeneous tissue elastic properties while some previous studies have assessed the effect of heterogeneous mineral density on the macroscopic stiffness of bone (Blanchard et al., 2013; Renders et al., 2008). Renders et al. (2008) found a decrease of 21% in apparent stiffness when considering mineral heterogeneity. However the effect of heterogeneities at the solid phase on finite element models with geometrical nonlinearities is still unclear. Since we wanted to be able to compare our macroscopic yield strains with previously published results, we kept our solid phase elastic properties as homogeneous.

The study assumes that the solid phase of bone can be modelled as a plastic material, which is not entirely true as high localised strains can cause microcracks and eventual fracture; effects that full plasticity based models may not be able to capture. Furthermore, we did not consider hardening (Carnelli et al., 2010) because there is no agreement on the hardening law at the scale of the solid phase we are considering. However, previous experimental and theoretical studies such as Schwiedrzik et al. (2014), Luczynski et al. (2015) and Fritsch et al. (2009) showed that the extracellular matrix of bone has a hardening behaviour after yield.

6. Conclusions

Trabecular bone has fairly uniform macroscopic yield behaviour across samples in normal strain space. Thus, modelling it by using strain-based plasticity makes sense. For tension-tension and compression-compression quadrants in normal strain space, the strain norm at yield shows little variation, indicating an isotropic behaviour in these regimes.

In the tension-compression quadrants, pure shear and combined normal-shear planes, the macroscopic strain norms at yield have a relatively large variation, indicating a possible absence of isotropy. Further, differences in yield strain values in clockwise and counter-clockwise shear may indicate a possible anisotropy for the macroscopic behaviour of trabecular bone. However, due to the difficulties of formulating a non-isotropic closed-form yield surface in strain space due to the weak relationships between fabric and yield strains, and due to the small difference in fitting errors between isotropic and orthotropic or anisotropic considerations, an isotropic criterion presents itself as the most suitable approximation. However, for some load cases, considerable differences between the closed-form yield criterion and the actual yield strain may arise.

With respect to the yield surface, an eccentric-ellipsoid may adequately represent the macroscopic yield surface of bone as the fitting errors for all the considered symmetries are reasonably small. However, it is important to be mindful of the asymmetry in shear yield strains and that in the normal-shear load cases, the quadric may not be able to represent the macroscopic yield behaviour of trabecular bone.

This work provides a comprehensive assessment of material symmetries of trabecular bone at the macroscale and describes in detail its macroscopic yield and its underlying microscopic mechanics.

Acknowledgements

The authors would like to thank EPSRC for providing access to ARCHER, UK National Supercomputing Service, through project e398, "Modelling nonlinear micromechanical behaviour of bone", and funding through the grant EP/K036939/1. We also would like to acknowledge The Hartree Centre, Science and Technology Facilities Council for access to Blue Joule through project HCP010 and funding from BBSRC through the grant BB/K006029/1. Additionally, the first author is grateful for the Principal's Career Development PhD Scholarship of the University of Edinburgh.

REFERENCES

Bayraktar, H.H., Gupta, A., Kwon, R.Y., Papadopoulos, P., Keaveny, T.M., 2004a. The modified super-ellipsoid yield criterion for human trabecular bone. J. Biomech. Eng. – T Asme 126, 677–684.

Bayraktar, H.H., Keaveny, T.M., 2004b. Mechanisms of uniformity of yield strains for trabecular bone. J. Biomech. 37, 1671–1678.

Bevill, G., Eswaran, S.K., Gupta, A., Papadopoulos, P., Keaveny, T. M., 2006. Influence of bone volume fraction and architecture on computed large-deformation failure mechanisms in human trabecular bone. Bone 39, 1218–1225.

Blanchard, R., Dejaco, A., Bongaers, E., Hellmich, C., 2013. Intravoxel bone micromechanics for microCT-based finite element simulations. J. Biomech. 46, 2710–2721.

Carnelli, D., Gastaldi, D., Sassi, V., Contro, R., Ortiz, C., Vena, P., 2010. A finite element model for direction-dependent mechanical response to nanoindentation of cortical bone allowing for anisotropic post-yield behavior of the tissue. J. Biomech. Eng. – T Asme, 132.

Chang, W.C.W., Christensen, T.M., Pinilla, T.P., Keaveny, T.M., 1999. Uniaxial yield strains for bovine trabecular bone are isotropic and asymmetric. J. Orthop. Res. 17, 582–585.

Completo, A., Simoes, J.A., Fonseca, F., 2009. Revision total knee arthroplasty: The influence of femoral stems in load sharing and stability. Knee 16, 275–279.

Conlisk, N., Howie, C.R., Pankaj, P., 2015. The role of complex clinical scenarios in the failure of modular components following revision total knee arthroplasty: a finite element study. J. Orthop. Res. 33, 1134–1141.

Cowin, S.C., 1986. Fabric dependence of an anisotropic strength criterion. Mech. Mater. 5, 251–260.

Cowin, S.C., 1997. Remarks on the paper entitled 'Fabric and elastic principal directions of cancellous bone are closely related'. J Biomech. 30, 1191–1192.

de Souza Neto, E.A., Blanco, P.J., Sanchez, P.J., Feijoo, R.A., 2015. An RVE-based multiscale theory of solids with micro-scale inertia and body force effects. Mech. Mater. 80, 136–144.

de Souza Neto, E.A., Peric, D., Owens, D., 2008. In: Computational methods for plasticity: theory and applications 1st ed. Wiley, Chichester, West Sussex, UK.

Donaldson, F.E., Pankaj, P., Cooper, D.M.L., Thomas, C.D.L., Clement, J.G., Simpson, A.H.R.W., 2011. Relating age and microarchitecture with apparent-level elastic constants: a micro-finite element study of female cortical bone from the anterior femoral midshaft. Proc. Inst. Mech. Eng. H 225, 585–596.

Doube, M., Klosowski, M.M., Arganda-Carreras, I., Cordelieres, F.P., Dougherty, R.P., Jackson, J.S., Schmid, B., Hutchinson, J.R., Shefelbine, S.J., 2010. BoneJ Free and extensible bone image analysis in Image. J. Bone 47, 1076–1079.

Falcinelli, C., Schileo, E., Balistreri, L., Baruffaldi, F., Bordini, B., Viceconti, M., Albisinni, U., Ceccarelli, F., Milandri, L., Toni, A., Taddei, F., 2014. Multiple loading conditions analysis can improve the association between finite element bone strength estimates and proximal femur fractures: A preliminary study in elderly women. Bone 67, 71–80.

Fenech, C.M., Keaveny, T.M., 1999. A cellular solid criterion for predicting the axial-shear failure properties of bovine trabecular bone. J. Biomech. Eng. – T Asme 121, 414–422.

Forum, M.P., 1994. MPI: A Message-Passing Interface Standard. University of Tennessee, Knoxville, Tennessee, USA.

Fritsch, A., Hellmich, C., Dormieux, L., 2009. Ductile sliding between mineral crystals followed by rupture of collagen crosslinks: Experimentally supported micromechanical explanation of bone strength. J. Theor. Biol. 260, 230–252.

Gibson, L.J., Ashby, M.F., 1997. Cellular solids: structure and properties, 2nd ed. Cambridge University Press, Cambridge, UK.

Gomez, W., Sales, E., Lopes, R.T., Pereira, W.C.A., 2013. A comparative study of automatic thresholding approaches for 3D x-ray microtomography of trabecular bone. Med. Phys., 40.

Harrigan, T.P., Jasty, M., Mann, R.W., Harris, W.H., 1988. Limitations of the continuum assumption in cancellous bone. J. Biomech. 21, 269–275.

Harrigan, T.P., Mann, R.W., 1984. Characterization of microstructural anisotropy in orthotropic materials using a 2nd rank tensor. J. Mater. Sci. 19, 761–767.

Helgason, B., Perilli, E., Schileo, E., Taddei, F., Brynjolfsson, S., Viceconti, M., 2008. Mathematical relationships between bone density and mechanical properties: A literature review. Clin. Biomech. 23, 135–146.

Hellmich, C., Ulm, F.J., Dormieux, L., 2004. Can the diverse elastic properties of trabecular and cortical bone be attributed to only a few tissue-independent phase properties and their interactions? Arguments from a multiscale approach. Biomech. Model. Mechanobiol. 2, 219–238.

Keaveny, T.M., Wachtel, E.F., Ford, C.M., Hayes, W.C., 1994. Differences between the tensile and compressive strengths of bovine tibial trabecular bone depend on modulus. J Biomech. 27, 1137–1146.

Keaveny, T.M., Wachtel, E.F., Zadesky, S.P., Arramon, Y.P., 1999. Application of the Tsai-Wu quadratic multiaxial failure criterion to bovine trabecular bone. J. Biomech. Eng. – T Asme 121, 99–107.

Keller, T.S., 1994. Predicting the compressive mechanical-behavior of bone. J. Biomech. 27, 1159–1168.

Kopperdahl, D.L., Keaveny, T.M., 1998. Yield strain behavior of trabecular bone. J. Biomech. 31, 601–608.

Kruch, S., Chaboche, J.L., 2011. Multi-scale analysis in elasto-viscoplasticity coupled with damage. Int. J. Plast. 27, 2026–2039.

Lambers, F.M., Bouman, A.R., Tkachenko, E.V., Keaveny, T.M., Hernandez, C.J., 2014. The effects of tensile-compressive loading mode and microarchitecture on microdamage in human vertebral cancellous bone. J. Biomech. 47, 3605–3612.

Levrero Florencio, F., Margetts, L., Manda, K., Pankaj, P., 2015. Massively Parallel Simulations Of The Nonlinear Mechanical Behaviour of Trabecular Bone. Congress of the European Society of Biomechanics, Prague, Czech Republic.

Luczynski, K.W., Steiger-Thirsfeld, A., Bernardi, J., Eberhardsteiner, J., Hellmich, C., 2015. Extracellular bone matrix exhibits hardening elastoplasticity and more than double cortical strength: Evidence from homogeneous compression of non-tapered single micron-sized pillars welded to a rigid substrate. J. Mech. Behav. Biomed. Mater. 52, 51–62.

Malandrino, A., Fritsch, A., Lahayne, O., Kropik, K., Redl, H., Noailly, J., Lacroix, D., Hellmich, C., 2012. Anisotropic tissue elasticity in human lumbar vertebra, by means of a coupled ultrasound-micromechanics approach. Mater. Lett. 78, 154–158.

Margetts, L., 2002. Parallel finite element analysis. University of Manchester, Manchester, UK.

Margetts, L., Arregui, J.D., Mummery, P.M., Evans, L.M., Shterenlikht, A., Levrero Florencio, F., Pankaj, P., 2015. Recent Progress

in the Massively Parallel Solution of Implicit Problems, Proceedings of the NAFEMS World Congress, San Diego, USA.
Matsuura, M., Eckstein, F., Lochmuller, E.M., Zysset, P.K., 2008. The role of fabric in the quasi-static compressive mechanical properties of human trabecular bone from various anatomical locations. Biomech. Model. Mech. 7, 27–42.
McDowell, D.L., 2010. A perspective on trends in multiscale plasticity. Int. J. Plast. 26, 1280–1309.
Mehrabadi, M.M., Cowin, S.C., 1990. Eigentensors of linear anisotropic elastic-materials. Q. J. Mech. Appl. Math. 43, 15–41.
Morgan, E.F., Bayraktar, H.H., Yeh, O.C., Majumdar, S., Burghardt, A., Keaveny, T.M., 2004. Contribution of inter-site variations in architecture to trabecular bone apparent yield strains. J. Biomech. 37, 1413–1420.
Morgan, E.F., Keaveny, T.M., 2001. Dependence of yield strain of human trabecular bone on anatomic site. J. Biomech. 34, 569–577.
Nalla, R.K., Kinney, J.H., Ritchie, R.O., 2003. Mechanistic fracture criteria for the failure of human cortical bone. Nat. Mater. 2, 164–168.
Odgaard, A., 1997. Three-dimensional methods for quantification of cancellous bone architecture. Bone 20, 315–328.
Odgaard, A., Hvid, I., Linde, F., 1989. Compressive Axial Strain Distributions in Cancellous Bone Specimens. J. Biomech. 22, 829–835.
Odgaard, A., Kabel, J., vanRietbergen, B., Dalstra, M., Huiskes, R., 1997. Fabric and elastic principal directions of cancellous bone are closely related. J. Biomech. 30, 487–495.
Pankaj, P., 2013. Patient-specific modelling of bone and bone-implant systems: the challenges. Int. J. Numer. Methods Biomed. Eng. 29, 233–249.
Pankaj, P., Donaldson, F.E., 2013. Algorithms for a strain-based plasticity criterion for bone. Int. J. Numer. Methods Biomed. Eng. 29, 40–61.
Panyasantisuk, J., Pahr, D.H., Zysset, P.K., 2015. Effect of boundary conditions on yield properties of human femoral trabecular bone. Biomech. Model. Mechanobiol..
Perez-Foguet, A., Armero, F., 2002. On the formulation of closest-point projection algorithms in elastoplasticity - part II: Globally convergent schemes. Int. J. Numer. Methods Eng. 53, 331–374.
Renders, G.A.P., Mulder, L., Langenbach, G.E.J., van Ruijven, L.J., van Eijden, T.M.G.J., 2008. Biomechanical effect of mineral heterogeneity in trabecular bone. J. Biomech. 41, 2793–2798.
Rincon-Kohli, L., Zysset, P.K., 2009. Multi-axial mechanical properties of human trabecular bone. Biomech. Model Mechanobiol. 8, 195–208.
Sanyal, A., Gupta, A., Bayraktar, H.H., Kwon, R.Y., Keaveny, T.M., 2012. Shear strength behavior of human trabecular bone. J. Biomech. 45, 2513–2519.
Sanyal, A., Scheffelin, J., Keaveny, T.M., 2015. The Quartic Piecewise-Linear Criterion for the Multiaxial Yield Behavior of Human Trabecular Bone. J. Biomech. Eng. – T Asme, 137.
Schileo, E., Dall'Ara, E., Taddei, F., Malandrino, A., Schotkamp, T., Baleani, M., Viceconti, M., 2008. An accurate estimation of bone density improves the accuracy of subject-specific finite element. J Biomech. 41 3294-3294.
Schwiedrzik, J., Gross, T., Bina, M., Pretterklieber, M., Zysset, P., Pahr, D., 2015. Experimental validation of a nonlinear muFE model based on cohesive-frictional plasticity for trabecular bone. Int. J. Numer. Method Biomed. Eng..
Schwiedrzik, J., Raghavan, R., Burki, A., LeNader, V., Wolfram, U., Michler, J., Zysset, P., 2014. In situ micropillar compression reveals superior strength and ductility but an absence of damage in lamellar bone. Nat. Mater. 13, 740–747.
Schwiedrzik, J.J., Wolfram, U., Zysset, P.K., 2013. A generalized anisotropic quadric yield criterion and its application to bone tissue at multiple length scales. Biomech. Model. Mechanobiol. 12, 1155–1168.
Smith, I.M., Griffiths, D.V., Margetts, L., 2014. In: Programming the finite element method 5th ed. Wiley, Chichester, West Sussex.
Smith, I.M., Margetts, L., 2003. Portable parallel processing for nonlinear problems, International Conference on Computational Plasticity, Barcelona, Spain.
Smith, I.M., Margetts, L., 2006. The convergence variability of parallel iterative solvers. Eng. Comput. 23, 154–165.
Stolken, J.S., Kinney, J.H., 2003. On the importance of geometric nonlinearity in finite-element simulations of trabecular bone failure. Bone 33, 494–504.
Tai, K., Ulm, F.J., Ortiz, C., 2006. Nanogranular origins of the strength of bone. Nano Lett. 6, 2520–2525.
Tassani, S., Ohman, C., Baruffaldi, F., Baleani, M., Viceconti, M., 2011. Volume to density relation in adult human bone tissue. J. Biomech. 44, 103–108.
Theocaris, P.S., 1992. Failure modes of closed-cell polyurethane foams. Int. J. Fract. 56, 353–375.
Tsai, S.W., Wu, E.M., 1971. General theory of strength for anisotropic materials. J. Compos. Mater. 5, 58–80.
Turner, C.H., Cowin, S.C., 1987. Dependence of elastic-constants of an anisotropic porous material upon porosity and fabric. J. Mater. Sci. 22, 3178–3184.
Turner, C.H., Cowin, S.C., Rho, J.Y., Ashman, R.B., Rice, J.C., 1990. The fabric dependence of the orthotropic elastic-constants of cancellous bone. J. Biomech. 23, 549–561.
van Buskirk, W.C., Cowin, S.C., Ward, R.N., 1981. Ultrasonic Measurement of Orthotropic Elastic-Constants of Bovine Femoral Bone. J. Biomech. Eng. – T Asme 103, 67–72.
van Rietbergen, B., Odgaard, A., Kabel, J., Huiskes, R., 1996. Direct mechanics assessment of elastic symmetries and properties of trabecular bone architecture. J. Biomech. 29, 1653–1657.
van Rietbergen, B., Weinans, H., Huiskes, R., Odgaard, A., 1995. A new method to determine trabecular bone elastic properties and loading using micromechanical finite-element models. J. Biomech. 28, 69–81.
Wang, C.Y., Feng, L., Jasiuk, I., 2009. Scale and boundary conditions effects on the apparent elastic moduli of trabecular bone modeled as a periodic cellular solid. J. Biomech. Eng. – T Asme, 131.
Wolfram, U., Gross, T., Pahr, D.H., Schwiedrzik, J., Wilke, H.J., Zysset, P.K., 2012. Fabric-based Tsai-Wu yield criteria for vertebral trabecular bone in stress and strain space. J. Mech. Behav. Biomed. 15, 218–228.
Wolfram, U., Wilke, H.J., Zysset, P.K., 2010. Rehydration of vertebral trabecular bone: Influences on its anisotropy, its stiffness and the indentation work with a view to age, gender and vertebral level. Bone 46, 348–354.
Zysset, P.K., Curnier, A., 1995. An Alternative Model for Anisotropic Elasticity Based on Fabric Tensors. Mech. Mater. 21, 243–250.